Syntheses and physical properties of the MAX phase boride Nb_2SB and the solid solutions $Nb_2SB_xC_{1-x}$ ($x = 0$–1)

Tobias Rackl, Lucien Eisenburger, Robin Niklaus, and Dirk Johrendt*
Department Chemie, Ludwig-Maximilians-Universität München, Butenandtstr. 5-13 (D), 81377 München, Germany

(Received 28 January 2019; revised manuscript received 2 April 2019; published 3 May 2019)

The MAX phase boride Nb_2SB and the solid solutions $Nb_2SB_xC_{1-x}$ ($x = 0$–1) were synthesized via solid-state methods and characterized by x-ray powder diffraction. All phases crystallize in the hexagonal Cr_2AlC type with the space group $P6_3/mmc$. The lattice parameters increase with the boron content [$a = 3.278(1) - 3.334(1)$ Å (+1.7%), $c = 11.49(1) - 11.54(1)$ Å (+0.5%)] and the distortions of the $Nb_6(B, C)$ octahedra slightly decrease. Magnetic susceptibility and dc resistivity measurements confirm that Nb_2SC is a superconductor while Nb_2SB shows no superconducting transition above 1.9 K. The solid solutions $Nb_2SB_xC_{1-x}$ are metals and superconductors for $x = 0$–0.6 with critical temperatures of $T_c = 4.8$–2.6 K, which decrease with increasing boron content. First-principles density-functional theory calculations confirm the metallic state and a lower electronic density of states at the Fermi energy in the boride. The calculated elastic constants, phonon density of states, and Debye temperatures of Nb_2SB are similar to Nb_2SC and are probably not the reason for the absence of superconductivity in the boride. We therefore suggest that the lower $N(\varepsilon_F)$ of the boride reduces the interaction strength and thus the superconducting critical temperature.

DOI: 10.1103/PhysRevMaterials.3.054001

I. INTRODUCTION

The MAX phases are a large family of layered ternary compounds with the chemical formula $M_{1+n}AX_n$ ($n = 1$–3), where M is an early transition metal, A is a main group element, and X is either carbon or nitrogen. Their hexagonal crystal structures consist of $M_{1+n}X_n$ layers interleaved with A-group element layers. Strong M–X bonds and weaker M–A bonds result in a nanolaminated structure. First synthesized by Nowotny *et al.* in the 1960s, they still attract great interest due to their unified metallic and ceramic properties [1]. This outstanding combination makes them promising candidates for a wide range of uses like sensors, electric contacts, and especially high-temperature applications [2–5].

More than 60 ternary MAX phases and a large number of solid solutions exist. Especially, the substitution of the M and A sites yielded various compounds, for example $(Nb, Zr)_2AlC$, $(Ti, V)_2SC$, $(Ti, Hf)_2SC$, $V_2(Al, Ga)C$, $Ti_2(Si, Ge)C$, and $Cr_2(Al, Ge)C$ [5–12]. In contrast, X-site solid solutions are mostly limited to carbonitrides $M_{n+1}A(C, N)_n$ up to now. One example is $Ti_2AlC_{0.5}N_{0.5}$ [13] with enhanced hardness and stiffness compared to Ti_2AlC and the nitride Ti_2AlN [14]. Oxygen can also incorporate into MAX phases, by either the reaction with gaseous O_2 or with Al_2O_3 [15,16]. However, the oxygen saturation content in $M_{n+1}A(C, O)_n$ is not known [3].

Even though the importance of the X atom on the properties of MAX phases is accepted, potential elements are currently restricted to carbon, nitrogen, and possibly oxygen. Recently, MAX borides have been theoretically predicted [17,18]. Among them, some M_2AlB (M = Sc, Ti, Cr, Zr, Nb, Mo, Hf, and Ta) phases should be metastable. Theoretical analysis of the mechanical properties showed that the predicted Ta_2AlB, Cr_2AlB, and Mo_2AlB exhibit high shear and Young's moduli, while Zr_2AlB is a great candidate for structural applications. Furthermore, *ab initio* calculations showed that among the M_2AB (M = Ti, Zr, Hf; A = Al, Ga, In) phases Hf_2InB is the most stable, although all compounds have negative formation enthalpies and should therefore be synthesizable [19]. A recent study compares V_2AlC with hypothetical V_2AlB, and predicts that boron-based MAX phases are more ductile due to weaker V–B bonds [20].

A family of compounds closely related to the MAX phases is called the MAB phases, wherein M is a transition metal, A is Al or Si, and B is boron. Although MAB and MAX phases show different structural motifs, they share the two-dimensionality and the combination of covalent and metallic interactions. MAB phases form layered structures in different orthorhombic space groups. Layers of face-sharing BM_6 trigonal prisms are alternately stacked with Al or Si [21–31]. The BM_6 prism is the common coordination polyhedra for binary transition-metal borides for example in Cr_2B_3, NbB_2, Nb_3B_4, ZrB_2, and many more [32–35].

In this paper we report the syntheses of the MAX phase boride Nb_2SB and its solid solutions with the carbide $Nb_2SB_xC_{1-x}$ ($x = 0$–1). These are the first MAX phase borides. The change of the crystal structure was studied by Rietveld refinement of x-ray powder-diffraction patterns. The substitution of carbon by boron can be tracked by the change of lattice parameters as well as by the distortion of the $Nb_6(B, C)$ octahedra. We show that the compounds $Nb_2SB_xC_{1-x}$ ($x = 0$–1) are metallic conductors and exhibit superconductivity for $x = 0$–0.6.

*johrendt@lmu.de

II. EXPERIMENTAL

Polycrystalline samples of $Nb_2SB_xC_{1-x}(x = 0–1)$ were synthesized by solid-state reaction of the elements niobium (99.99 %, ~325 mesh, Alfa Aesar), sulfur (⩾99 %, flakes, Sigma Aldrich), boron (99 %, powder, Koch-Light-Laboratories), and graphite (100 %, powder, ACROS Organics). For microwave reaction, a homogenized mixture of niobium and sulfur with the ratio 2:1 was filled in an alumina crucible and sealed in an argon-filled silica tube. The ampoule was placed in an alumina crucible, which was filled with 25-g granular graphite. An insulating housing surrounded the setup. The reaction took place at 600 W for 20 min. After cooling down to room temperature, the obtained black powder was homogenized and used for the following reactions. A mixture of the prereacted niobium-sulfur, boron, and carbon was homogenized and pressed to a pellet with a diameter of 5 mm (2 t, 120 s). The pellet was welded in an argon-filled niobium crucible and then sealed in an argon-filled silica tube. The reaction mixture was heated to 1200 °C within 6 h and a 65-h dwell time. The crucibles were allowed to cool down to room temperature by shutting off the oven. The procedure was repeated 2–5 times to increase the homogeneity of the samples. The products were black powders with purities of 92–99 wt %.

Powder x-ray diffraction was carried out using a Huber G670 diffractometer with Cu-Kα_1 radiation ($\lambda = 1.54059$ Å) and Ge-111 monochromator. Structural parameters were determined by Rietveld refinement using the TOPAS software package [36]. Magnetic and resistivity measurements were performed with a Quantum Design PPMS-9. The magnetization was determined using the vibrating sample magnetometer option. Zero-field-cooled and field-cooled measurements were carried out between 1.9 and 20 K with an applied field of 15 Oe. The isothermal magnetization was determined at 1.9 K with variable fields of $H = \pm 50$ kOe. For resistivity measurements, the samples were pressed to pellets with a diameter of 5 mm and a thickness of ~1 mm. The pellets were sintered at 1000 °C for 48 h and contacted using the Wimbush press contact assembly for van der Pauw measurements [37].

For scanning transmission electron microscopy (STEM) a small volume of the sample was ground in absolute ethanol. The resulting suspension was applied to a copper grid covered with holey carbon film (Plano GmbH, Germany). The grid was mounted on a double-tilt holder and transferred into a C_s dodecapole corrector probe-corrected Titan Themis 300 (FEI, USA) TEM equipped with an extreme field emission gun, a postcolumn filter (Enfinium ER-799), an US1000XP/FT camera system (Gatan, Germany), and a windowless four-quadrant Super-X energy dispersive x-ray spectroscopy detector. TEM images were recorded using a 4k × 4k FEI Ceta complementary metal-oxide semiconductor camera. The microscope was operated at 300-kV accelerating voltage for SAED and STEM-HAADF (convergence angle of 16.6 mrad, 50-μm aperture, detector inner half angle 63 mrad for 100-mm camera length). For evaluation of the TEM data Digital Micrograph (Fourier filtering of STEM images) was used.

Electronic structure calculations were performed using the Vienna *Ab initio* Simulation Package (VASP) [38,39], which is based on density-functional theory (DFT) and plane-wave basis sets. Projector-augmented waves (PAW) [40] were used and contributions of correlation and exchange were treated in the generalized-gradient approximation [41]. The PAW eigenstates were afterward projected onto localized crystal orbitals using LOBSTER [42]. Elastic tensors were determined by performing finite distortions and deriving the elastic constants from the strain-stress relationship. The bulk modules were calculated using the Voigt approximation $B = (1/9)[(C_{11} + C_{12}) + 4C_{13} + C_{33}]$ or from energy vs volume calculations which yielded the same results. Debye temperatures Θ_D were estimated from the bulk modules and Poisson ratios using a quasiharmonic model [43]. For phonon calculations of 2 × 2 × 2 supercells were calculated with a k-mesh sampling of 8 × 8 × 3. Force sets and lattice vibrations were subsequently calculated using the PHONOPY program [44,45]. Further details are provided in the Supplemental Material [46].

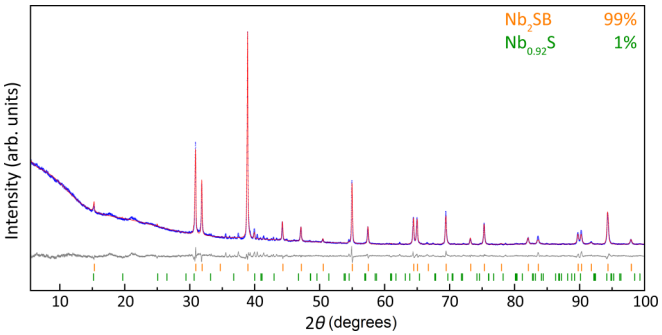

FIG. 1. X-ray powder pattern of Nb_2SB (blue) with Rietveld fit (red) and difference curve (gray).

III. RESULTS AND DISCUSSION

A. Synthesis and crystal structure

Nb_2SB and its solid solutions with carbon $Nb_2SB_xC_{1-x}(x = 0–1)$ can be synthesized at 1200 °C via solid-state reaction. It turned out that the use of a prereacted mixture of niobium and sulfur in the ratio of 2:1 leads faster to the product than the direct use of the elements. The prereaction took place in a microwave oven, as a fast and efficient way to prepare precursors. Besides the prereaction, a rapid cooling rate also prefers the formation of $Nb_2SX(X = B, C)$ phases. Samples with broad reflections in the powder-diffraction pattern or a significant amount of impurity phases were homogenized and heated again under the same conditions. The $Nb_2SB_xC_{1-x}(x = 0–1)$ phases prepared by this procedure are black powders. The proportions of the products are >92 wt % with the impurity phases NbC and NbB. Minor unidentified impurities occur for $x \geqslant 0.80$.

Figure 1 shows the Rietveld refinement of the powder-diffraction pattern of Nb_2SB starting from the Nb_2SC structure. Nb_2SB crystallizes in the hexagonal space group $P6_3/mmc$ (see Table I) just as the solid solutions $Nb_2SB_xC_{1-x}(x = 0–1)$. Layers of edge-sharing $Nb_6(C, B)$ octahedra alternate with sulfur layers (Fig. 2). The unit-cell

TABLE I. Crystallographic data of Nb_2SB.

Chemical formula	Nb_2SB
M(g · mol^{-1})	228.69
Crystal system, space group	hexagonal, $P6_3/mmc$ (194)
T (K)	293
a (Å), c (Å)	3.335(1), 11.55(1)
V (Å^3)	111.2(1)
Z	2
Radiation type	Cu $K_{\alpha1}$, $\lambda = 1.54056$ Å
Diffractometer	Huber G670
Monochromator	Ge-111
R_p	2.290
R_{wp}	3.447
Goodness of fit	3.709

Atom positions and equivalent isotropic displacement parameters (Å^2)

Atom	x	y	z	U_{eq}	occ
Nb	1/3	2/3	0.60172 (6)	0.5	1
S	1/3	2/3	1/4	1	1
B	0	0	0	3	1

Selected interatomic distances (Å)

B—6 × Nb 2.2557(4) S—6 × Nb 2.5772(5) Nb—3 × Nb 3.0383(8)

dimensions of Nb_2SB are slightly enlarged with $a = 3.335(1)$ Å, $c = 11.55(1)$ Å, and $V = 111.2(1)$ Å^3 compared to Nb_2SC ($a = 3.278(1)$ Å, $c = 11.49(1)$ Å, and $V = 107.0(1)$ Å^3).

Figure 3 shows a STEM-HAADF image of Nb_2SB perpendicular to [100]. The brightest intensity can be assigned to niobium atoms and the crystal structure is superimposed to the image. The "zigzag" stacking of the MB_6 octahedral layers is characteristic for MAX phases [3].

Nb_2SC_x($x = 0.66$–1) is different from most ternary MAX phases, because it shows significant vacancies at the C site, which shortens the a axis with decreasing x [47]. It might be that the vacancies in this system open the opportunity to substitute carbon by boron.

Since it is not possible to determine a C/B mixed occupancy at the X site with the Rietveld method, different parameters are necessary to track the degree of substitution in $Nb_2SB_xC_{1-x}$. One option is the change of the unit-cell dimensions. In solid solutions $Nb_2SB_xC_{1-x}$($x = 0$–1) the a axis increases by 1.7% with the boron content from 3.278(1) to 3.335(1) Å. In comparison, the elongation of the c axis from 11.49(1) to 11.55(1) Å ($\triangleq 0.5\,\%$) is less pronounced.

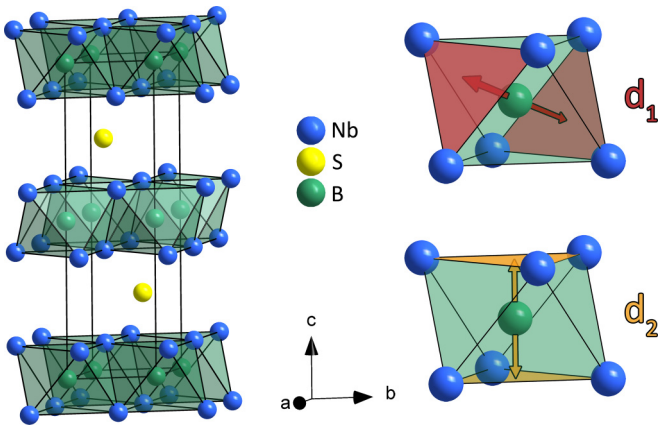

FIG. 2. Crystal structure of Nb_2SB (left). The plane distances d_1 (faces not parallel to the basal plane) and d_2 (faces parallel to the basal plane) used for the calculation of the octahedral distortion are displayed on the right.

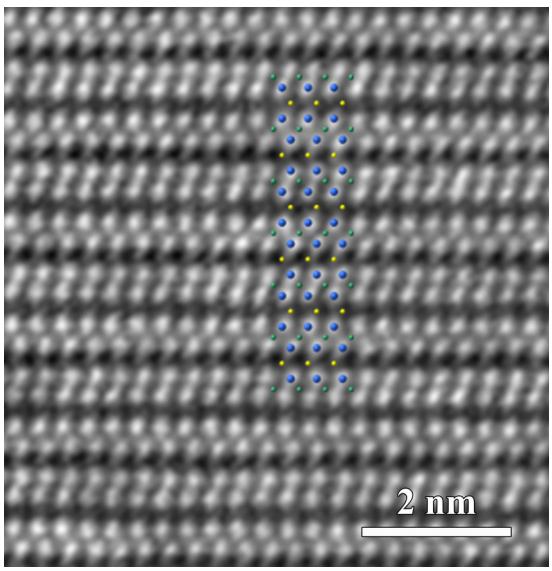

FIG. 3. STEM-HAADF image of Nb_2SB perpendicular to [100]. The inset of the structure of Nb_2SB indicates the position of Nb- (blue), S- (yellow), and B (green) atoms.

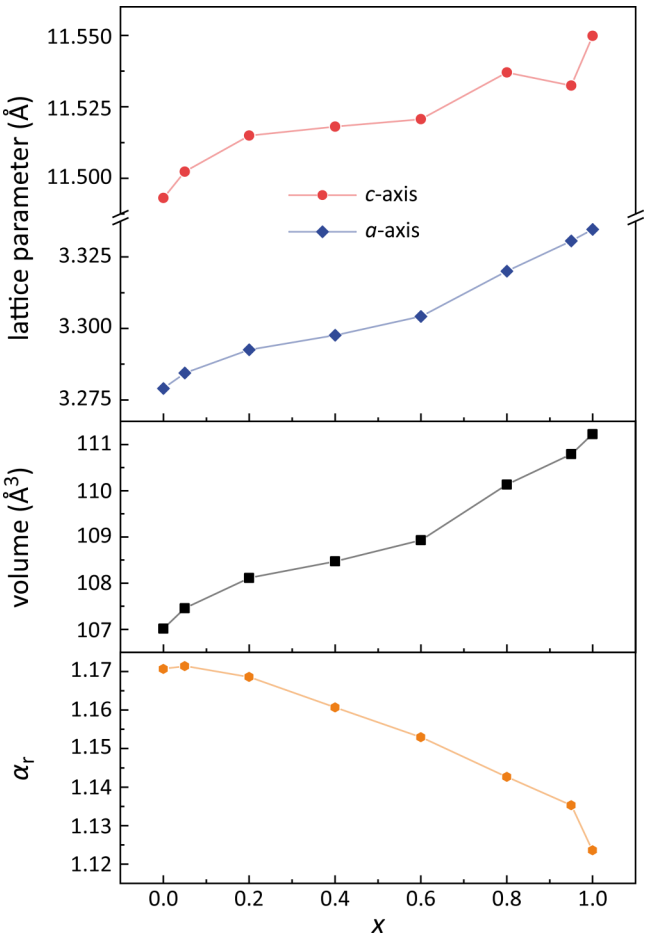

FIG. 4. Lattice parameters (top), unit-cell volume (middle), and octahedron aspect ratio (bottom) of $Nb_2SB_xC_{1-x}(x = 0–1)$ as a function of the boron content x.

The change of the a and c axis results in an increase of the cell volume by 3.9 % from 107.0(1) Å^3 to 111.2(1) Å^3 (see Fig. 4).

Another quantity to describe the change of the crystal structure is the distortion of the M_6X octahedron. Barsoum and co-workers [48] described the degree of distortion (α_r) by the ratio of the distance of two opposite faces not in the basal plane (d_1) and the distances of two opposite faces in the basal plane (d_2) (see Fig. 2). By rearranging the formula, the ratio depends on the coordinate z_M of the M atom and the c/a ratio [see Eq. (1)].

$$\alpha_r = \frac{d_1}{d_2} = \frac{\sqrt{3}}{2\sqrt{4z_M^2\left(\frac{c}{a}\right)^2 + \frac{1}{12}}} \quad (1)$$

Figure 4 displays the values α_r for the solid solutions $Nb_2SB_xC_{1-x}(x = 0–1)$. The octahedra become less distorted with increasing boron content, resulting in values of α_r from 1.171 to 1.123, which is a reduction of the distortion by 4.1%. The d_1/d_2 ratios are greater than 1, which means that the faces in the basal plane are closer together than the faces not in the basal plane. Since z_M increases by 5.8% while the c/a ratio decreases by 1.2%, the relaxation of the octahedron is a result of the z_M parameter of the Nb site and not the lattice

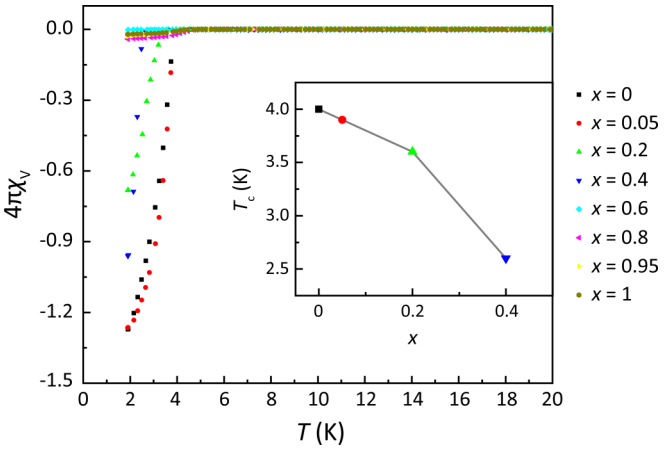

FIG. 5. Low-field (15 Oe) magnetic susceptibilities of $Nb_2SB_xC_{1-x}(x = 0–1)$ in the temperature range of 1.9 and 20 K. Inset: Critical temperature T_c as a function of the boron content in the solid solutions $Nb_2SB_xC_{1-x}(x = 0–1)$.

parameters. The substitution of carbon by boron reduces the Nb-Nb distance by 2.3% and thus the layer distances. The combination of both the octahedron relaxation and the layer compression leads to an almost unchanged c axis.

B. Magnetic properties

The susceptibility of $Nb_2SB_xC_{1-x}(x = 0–1)$ was measured in an external field of $H = 15$ Oe between 1.9 and 20 K. Isothermal magnetization plots at $T = 1.9$ K at variable fields of $H = \pm 50$ kOe are given in Supplemental Material, Figs. 9S-16S [46]. Figure 5 shows the susceptibility of $Nb_2SB_xC_{1-x}(x = 0–1)$. Bulk superconductivity occurs in Nb_2SC at the critical temperature $T_c = 4.0$ K, which is slightly lower than given in the literature [47]. T_c decreases from 4.0 to 2.6 K with increasing boron content from $x = 0–0.40$. For compounds with a higher boron content ($x \geqslant 0.60$), no bulk superconductivity is observed. For $x =$ 0.80, 0.95, and 1.0 the susceptibility drops slightly between 4 and 5 K, which indicates small amounts of unidentified superconducting impurities.

C. Resistivity

Figure 6 shows the temperature-dependent resistivity of the solid solutions $Nb_2SB_xC_{1-x}(x = 0–1)$. The values at room temperature are in the range of 1.3–4.5 $\times 10^{-6}$ Ωm with Nb_2SB showing the lowest resistivity, which is slightly higher than typical values of other MAX phases around 0.2–0.7 $\times$ 10^{-6} Ωm [3,49]. We also see no trend with the boron content x. However, resistivities of compacted polycrystalline samples strongly depend on hardly controllable grain-boundary effects, which make absolute values often unreliable. Between 50 and 300 K the resistivity decreases linearly with decreasing temperature, which is typical for metallic conductors.

The drop of resistance at low temperatures confirms the superconductivity of $Nb_2SB_xC_{1-x}$ ($x = 0–0.40$), which was also found in the magnetic measurements. The inset in Fig. 6 shows the dependence of T_c on x. As for the susceptibility data (Fig. 5), the critical temperature decreases with increasing

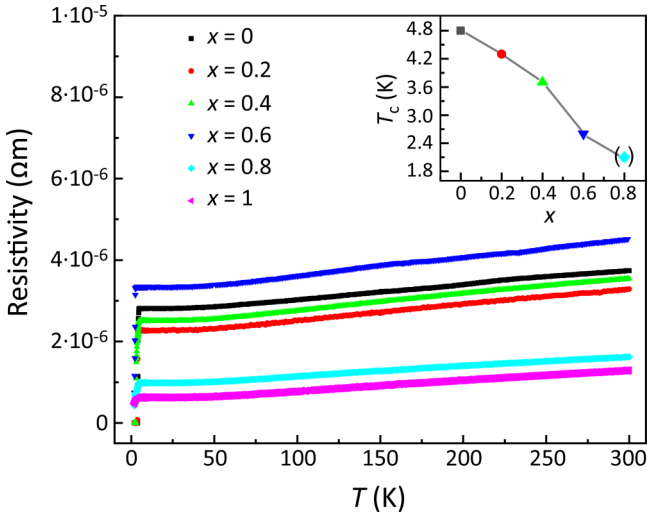

FIG. 6. Resistivities determined by van der Pauw measurements in the temperature range of 1.9 and 300 K. Inset: Critical temperature T_c as a function of the boron content in the solid solutions $Nb_2SB_xC_{1-x}$ ($x = 0$–1).

boron content. However, all values are slightly higher than those from the susceptibility data. $Nb_2SB_{0.6}C_{0.4}$ still exhibits superconductivity at $T_c = 2.6$ K. For $x = 0.80$ and 1.0 a drop occurs, but zero resistivity is not reached. This drop is a sign for superconducting impurity phases, which confirms the findings of the magnetic measurements.

Superconductivity in MAX phases is a rare phenomenon and there are conflicting reports whether some of them, for example Nb_2SnC, are superconductors or not [50]. Measurements of superconductivity are sensitive to impurity phases, which was shown in detail by Anasori *et al.* [51]. Studies in systems containing niobium are especially problematic, since the metal and some of its compounds, for example NbC, exhibit superconductivity. Our measurements clearly show Nb_2SC is a superconductor as described in the literature, while Nb_2SB it not superconducting above 1.9 K.

IV. ELECTRONIC AND ELASTIC PROPERTIES

First-principles DFT band-structure calculations confirm the metallic state of Nb_2SB. Figure 7(a) shows the total and atom-resolved density of states. The Nb 4*d* states dominate the density of state (DOS) at Fermi energy while contributions from sulfur and boron are small. Niobium states spread over more than 15 eV, which indicates strong covalent interactions with the boron and sulfur neighbors. Integration of the atom-resolved DOS gives the charges $(Nb^{+0.9})_2S^{-0.6}B^{-1.2}$ which covers the complete electron density thanks to the projection of the PAW eigenstates onto localized orbitals [42].

Figure 7(b) compares the total DOS of Nb_2SB and Nb_2SC. The band filling is larger in the carbide due to two additional electrons in the unit cell. Since the Fermi level is at a rising edge of the Nb dominated area, an increasing band filling also increases the density of states at the Fermi level $N(\varepsilon_F)$. By assuming that Nb_2SC is a conventional superconductor, the decreasing $N(\varepsilon_F)$ with boron substitution may be responsible for the lower critical temperatures of $Nb_2SB_xC_{1-x}$ and finally

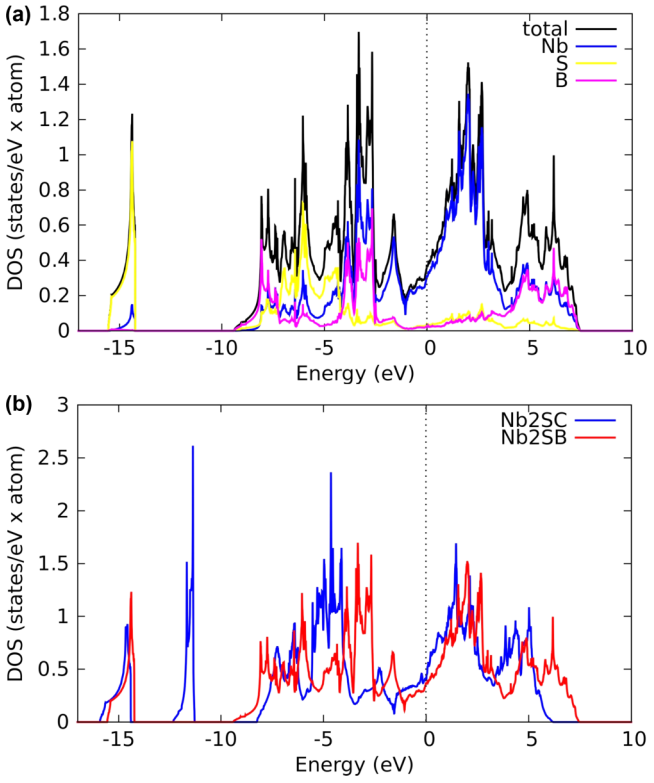

FIG. 7. (a) Total and atom-resolved density of states of Nb_2SC. (b) Total DOS of Nb_2SB in comparison with Nb_2SC, showing the lower DOS at the Fermi level in the boride. The energy zeros are taken at the Fermi level.

the absence of superconductivity in Nb_2SB. However, T_c of conventional superconductors also depends on the electron-phonon coupling strengths and the Debye temperature. These properties are linked to the elastic constants, which are available for Nb_2SC in the literature [52,53]. We have calculated the elastic constants, bulk moduli, linear compressibility ratios $f = k_c/k_a$, and the Debye temperatures for Nb_2SC and Nb_2SB. A comparison of the results is given in Table II.

The values for Nb_2SC from the literature and our calculation agree within 5–10%, which is probably due to the usage of different program packages, parameters, or potentials. Our results for Nb_2SC and Nb_2SB are comparable because they were calculated with the identical procedure. The elastic constants of the boride and carbide are similar, only the C_{44} values differ by 20 %. The boride has a slightly smaller bulk module but a higher Debye temperature compared to the carbide. From this one would expect a slightly higher superconducting

TABLE II. Elastic constants C_{ij} (GPa), bulk moduli B (GPa), compressibility ratios f, and Debye temperatures Θ_D (K) of Nb_2SC and Nb_2SB.

	C_{11}	C_{12}	C_{13}	C_{33}	C_{44}	B	f	Θ_D	Ref.
Nb_2SC	304	117	155	316	88	221	0.69		[52]
	320	101	153	327	126	197	0.66	540	[53]
	301	105	157	314	116	194	0.59	521	This work
Nb_2SB	316	95	131	317	143	186	0.80	573	This work

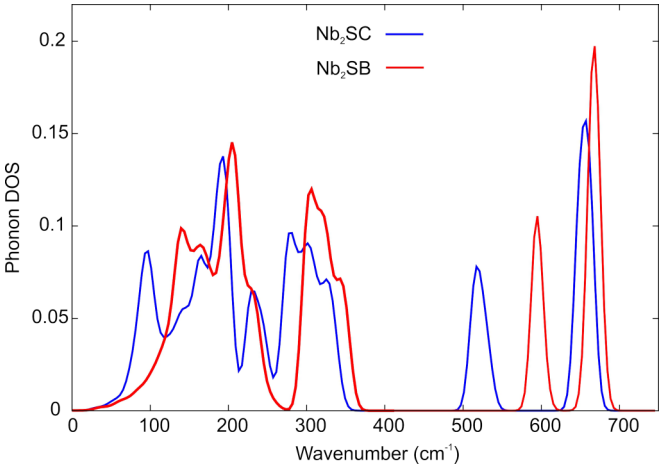

FIG. 8. Phonon density of states of Nb_2SC (blue) and Nb_2SB (red).

T_c in the boride, which contradicts the experimental finding. The compressibility ratio f shows that the a axis is softer in both compounds. This anisotropy is weaker in the boride where the f parameter is closer to 1.

Figure 8 shows the phonon density of states of Nb_2SB and Nb_2SC. The peaks at high frequencies between 500 and 700 cm^{-1} are caused by boron and carbon; sulfur modes are around 300 cm^{-1} and the broad feature around 100–250 cm^{-1} are niobium modes (for plots of the atom-projected phonon DOS see Fig. 17S in the Supplemental Material [46]).

All modes of the boride slightly shift to higher energies, which agrees with the higher calculated Debye temperature. This should increase T_c of the boride, which contradicts the experiments. A further analysis requires calculations of the electron-phonon coupling constants λ. Reference [53] classifies Nb_2SC as moderately coupled superconductor and estimates $\lambda = 0.49$ from the calculated $\Theta_D = 540$ K and the experimental $T_c = 4.8$ K using McMillan's formula [54]. Given that a T_c of Nb_2SB is below 1.9 K, the same formula with $\Theta_D = 570$ K gives $\lambda \leqslant 0.4$ as the upper limit for the boride. However, current methods to calculate λ [55] still comprise approximations, which make it very difficult to reliably discriminating a T_c difference of 3 K, especially in compounds with anisotropic crystal structures. In the present case, the Debye temperatures differ by only 10 %, which is within the uncertainty of the calculation, and would anyway change T_c by less than 0.5 K. On the other hand, $N(\varepsilon_F)$ is unambiguously smaller in the boride because it is an inevitable consequence of the lower band filling [Fig. 7(b)]. Given that λ roughly corresponds to the interaction strength $N(\varepsilon_F)V$ (V is the pairing potential) [54], we suggest that the lower T_c of the boride is finally a consequence of the lower density of states at the Fermi level.

V. CONCLUSIONS

Nb_2SB and the solid solutions $Nb_2SB_xC_{1-x}$($x = 0$–1) were successfully synthesized via solid-state methods. These are the first MAX phase borides. They crystallize in a layered hexagonal structure (Cr_2AlC type), which is characteristic for these phases. The carbon substitution by boron leads to increasing cell dimensions and to less distorted $Nb_6(B, C)$ octahedra. Nb_2SB is not a superconductor while Nb_2SC is superconducting below 5 K as described in the literature [48,56]. The solid solutions $Nb_2SB_xC_{1-x}$ are metallic conductors and exhibit superconductivity for $x = 0$–0.60, while T_c decreases with the boron content from 4.8 to 2.6 K. DFT calculations indicate the lowering of the density of states with increasing boron content, which we believe is the main reason for the decreasing critical temperatures. The elastic constants and Debye temperatures of the boride are similar and cannot account for the absence of superconductivity in the boride. We therefore suggest that the lower $N(\varepsilon_F)$ of the boride reduces the interaction strength and thus the superconducting critical temperature. Since $Nb_2SB_xC_{1-x}$($x = 0$–1) are among the first boron-containing MAX phases, the effects of boron on other properties like stiffness, thermal conductivity, shock resistance, damage tolerance, and electron-phonon coupling will be tasks for further investigations.

ACKNOWLEDGMENTS

We thank Professor Dr. Ján Minár for computing resources, and Professor Dr. Wolfgang Schnick for access to the STEM facilities. Financial support by the German Research Foundation (DFG, Grant No. JO257/7) is gratefully acknowledged.

[1] H. Nowotny, Prog. Solid State Chem. **5**, 27 (1971).
[2] A. S. Ingason, M. Dahlqvist, and J. Rosen, J. Phys.: Condens. Matter **28**, 433003 (2016).
[3] P. Eklund, M. Beckers, U. Jansson, H. Högberg, and L. Hultman, Thin Solid Films **518**, 1851 (2010).
[4] M. Radovic and M. W. Barsoum, Am. Ceram. Soc. Bull. **92**, 20 (2013).
[5] T. Cabioch, P. Eklund, V. Mauchamp, M. Jaouen, and M. W. Barsoum, J. Eur. Ceram. Soc. **33**, 897 (2013).
[6] M. Radovic, M. W. Barsoum, A. Ganguly, T. Zhen, P. Finkel, S. R. Kalidindi, and E. Lara-Curzio, Acta Mater. **54**, 2757 (2006).
[7] J. C. Schuster, H. Nowotny, and C. Vaccaro, J. Solid State Chem. **32**, 213 (1980).
[8] M. W. Barsoum, I. Salama, T. El-Raghy, J. Golczewski, H. J. Seifert, F. Aldinger, W. D. Porter, and H. Wang, Metall. Mater. Trans. A **33**, 2775 (2002).
[9] I. Salama, T. El-Raghy, and M. W. Barsoum, J. Alloys Compd. **347**, 271 (2002).
[10] S. Gupta and M. W. Barsoum, J. Electrochem. Soc. **151**, D24 (2004).
[11] H. Yang, B. Manoun, R. T. Downs, A. Ganguly, and M. W. Barsoum, J. Phys. Chem. Solids **67**, 2512 (2006).

[12] B. Manoun, S. K. Saxena, G. Hug, A. Ganguly, E. N. Hoffman, and M. W. Barsoum, J. Appl. Phys. **101**, 113523 (2007).
[13] M. W. Barsoum, T. El-Raghy, and M. Ali, Metall. Mater. Trans. A **31**, 1857 (2000).
[14] M. A. Pietzka and J. C. Schuster, J. Am. Ceram. Soc. **79**, 2321 (1996).
[15] O. Wilhelmsson, J. P. Palmquist, E. Lewin, J. Emmerlich, P. Eklund, P. O. Å. Persson, H. Högberg, S. Li, R. Ahuja, O. Eriksson, L. Hultman, and U. Jansson, J. Cryst. Growth **291**, 290 (2006).
[16] J. Rosen, P. O. Å. Persson, M. Ionescu, A. Kondyurin, D. R. McKenzie, and M. M. M. Bilek, Appl. Phys. Lett. **92**, 064102 (2008).
[17] M. Khazaei, M. Arai, T. Sasaki, M. Estili, and Y. Sakka, J. Phys.: Condens. Matter **26**, 505503 (2014).
[18] A. Gencer and G. Surucu, Mater. Res. Express **5**, 076303 (2018).
[19] G. Surucu, Mater. Chem. Phys. **203**, 106 (2018).
[20] P. Chakraborty, A. Chakrabarty, A. Dutta, and T. Saha-Dasgupta, Phys. Rev. Mater. **2**, 103605 (2018).
[21] M. Ade and H. Hillebrecht, Inorg. Chem. **54**, 6122 (2015).
[22] Y. Bai, X. Qi, A. Duff, N. Li, F. Kong, X. He, R. Wang, and W. E. Lee, Acta Mater. **132**, 69 (2017).
[23] Z. Guo, J. Zhou, and Z. Sun, J. Mater. Chem. A **5**, 23530 (2017).
[24] S. Kota, M. Agne, E. Zapata-Solvas, O. Dezellus, D. Lopez, B. Gardiola, M. Radovic, and M. W. Barsoum, Phys. Rev. B **95**, 144108 (2017).
[25] J. Lu, S. Kota, M. W. Barsoum, and L. Hultman, Mater. Res. Lett. **5**, 235 (2017).
[26] Y. Zhou, H. Xiang, F.-Z. Dai, and Z. Feng, Mater. Res. Lett. **5**, 440 (2017).
[27] S. Hirt, F. Hilfinger, and H. Hillebrecht, Z. Kristallogr. **233**, 295 (2018).
[28] S. Kota, Y. Chen, J. Wang, S. J. May, M. Radovic, and M. W. Barsoum, J. Eur. Ceram. Soc. **38**, 5333 (2018).
[29] L. Verger, S. Kota, H. Roussel, T. Ouisse, and M. W. Barsoum, J. Appl. Phys. **124**, 205108 (2018).
[30] Y. Bai, D. Sun, N. Li, F. Kong, X. Qi, X. He, R. Wang, and Y. Zheng, Int. J. Refract. Met. Hard Mater. **80**, 151 (2019).
[31] H. Zhang, F.-z. Dai, H. Xiang, Z. Zhang, and Y. Zhou, J. Mater. Sci. Technol. **35**, 530 (2019).
[32] R. Kessling, Acta Chem. Scand. **3**, 90 (1949).
[33] J. T. Norton, H. Blumenthal, and S. J. Sindeband, T. Am. I. Min. Met. Eng. **185**, 749 (1949).
[34] H. Nowotny, F. Benesovsky, and R. Kieffer, Z. Metallkd. **50**, 417 (1959).
[35] S. Okada, T. Atoda, I. Higashi, and Y. Takahashi, J. Less-Common Met. **113**, 331 (1985).
[36] A. Coelho, TOPAS-Academic, Coelho Software, Version 4.1, 2007.
[37] L. J. v. d. Pauw, Philips Tech. Rev. **20**, 220 (1958).
[38] G. Kresse and J. Furthmüller, Comput. Mater. Sci. **6**, 15 (1996).
[39] G. Kresse and D. Joubert, Phys. Rev. B **59**, 1758 (1999).
[40] P. E. Blöchl, Phys. Rev. B **50**, 17953 (1994).
[41] J. P. Perdew, K. Burke, and M. Ernzerhof, Phys. Rev. Lett. **77**, 3865 (1996).
[42] S. Maintz, V. L. Deringer, A. L. Tchougréeff, and R. Dronskowski, J. Comput. Chem. **34**, 2557 (2013).
[43] J. Brgoch, S. P. DenBaars, and R. Seshadri, J. Phys. Chem. C **117**, 17955 (2013).
[44] V. L. Deringer, R. P. Stoffel, A. Togo, B. Eck, M. Meven, and R. Dronskowski, CrystEngComm. **16**, 10907 (2014).
[45] A. Togo and I. Tanaka, Scr. Mater. **108**, 1 (2015).
[46] See Supplemental Material at http://link.aps.org/supplemental/10.1103/PhysRevMaterials.3.054001 for further crystallographic data, x-ray powder patterns of all compounds, magnetization data, and details of the phonon calculations.
[47] K. Sakamaki, H. Wada, H. Nozaki, Y. Ōnuki, and M. Kawai, Solid State Commun. **112**, 323 (1999).
[48] G. Hug, M. Jaouen, and M. W. Barsoum, Phys. Rev. B **71**, 024105 (2005).
[49] T. H. Scabarozi, S. Amini, P. Finkel, O. D. Leaffer, J. E. Spanier, M. W. Barsoum, M. Drulis, H. Drulis, W. M. Tambussi, J. D. Hettinger, and S. E. Lofland, J. Appl. Phys. **104**, 033502 (2008).
[50] P. Eklund, J. Rosen, and P. O. A. Persson, J. Phys. D: Appl. Phys. **50**, 113001 (2017).
[51] B. Anasori, M. Dahlqvist, J. Halim, E. J. Moon, J. Lu, B. C. Hosler, E. A. N. Caspi, S. J. May, L. Hultman, P. Eklund, J. Rosén, and M. W. Barsoum, J. Appl. Phys. **118**, 094304 (2015).
[52] I. R Shein and A. L. Ivanovskii, Phys. Status Solidi B **248**, 228 (2011).
[53] M. T. Nasir and A. K. M. A. Islam, Comput. Mater. Sci. **65**, 365 (2012)
[54] W. L. McMillan, Phys. Rev. **167**, 331 (1968).
[55] F. Giustino, Rev. Mod. Phys. **89**, 015003 (2017).
[56] K. Sakamaki, H. Wada, H. Nozaki, Y. Onuki, and M. Kawai, Mol. Cryst. Liq. Cryst. Sci. Technol., Sect. A **341**, 99 (2000).